International Journal of Applied Earth Observation and Geoinformation 12 (2010) 278–286

Contents lists available at ScienceDirect

International Journal of Applied Earth Observation and Geoinformation

journal homepage: www.elsevier.com/locate/jag

Universal reconstruction method for radiometric quality improvement of remote sensing images

Huanfeng Shen[a], Yaolin Liu[a], Tinghua Ai[a,*], Yi Wang[b], Bo Wu[c]

[a] School of Resource and Environmental Science, Wuhan University, 129 Luoyu Road, Wuhan 430079, Hubei, China
[b] Institute of Geophysics and Geomatics, China University of Geosciences, Wuhan, China
[c] Key Lab of Spatial Data Mining & Information Sharing of Ministry of Education, Fuzhou University, Fuzhou, China

ARTICLE INFO

Article history:
Received 28 July 2009
Accepted 6 April 2010

Keywords:
Remote sensing image
Radiometric quality improvement
Universal reconstruction method

ABSTRACT

The performance of remote sensing images in some applications is often affected by the existence of noise, blurring, stripes and corrupted pixels, as well as the hardware limits of the sensor with respect to spatial resolution. This paper presents a universal reconstruction method that can be used to improve the image quality by performing image denoising, deconvolution, destriping, inpainting, interpolation and super-resolution reconstruction. The proposed method consists of two parts: a universal image observation model and a universal image reconstruction model. In the observation model, most degradation processes in remote sensing imaging are considered in order to relate the desired image to the observed images. For the reconstruction model, we use the maximum *a posteriori* (MAP) framework to set up the minimization energy equation. The likelihood probability density function (PDF) is constructed based on the image observation model, and a robust Huber–Markov model is employed as the prior PDF. Experimental results are presented to illustrate the effectiveness of the proposed method.

1. Introduction

It is well known that remote sensing imagery can be applied in many fields, including mapping land-use and cover, agriculture, soils mapping, forestry, city planning, archaeological investigations, military observation and geomorphological surveying. In many cases, however, the performance of remote sensing images in these applications is affected by some degradations of image quality, such as the effects of random noise, sensor and/or atmosphere blurring, periodic stripes and corrupted pixels caused by damage of detector elements. These make it more difficult to visually and automatically interpret the remote sensing data. Besides, the spatial resolution of a remote sensing image is often not high enough for some applications due to the hardware limits of the imaging sensor. In order to improve image quality and increase application potential, implementing some digital image processing techniques is a commonly used procedure. The related techniques include image denoising, image deconvolution, image destriping, image inpainting, image interpolation and super-resolution (SR) reconstruction.

The goal of image denoising is to recover the original image from a noisy measurement. To denoise a remote sensing image, some adaptive filters such as the Lee filter (Lee, 1980), Kuan filter (Kuan et al., 1985), Frost filter (Frost et al., 1982) and their variations have commonly been embedded in commercial remote sensing software. For high-performance denoising techniques, the MAP (maximum *a posteriori*) (Isar et al., 2006; Achim et al., 2003) and wavelet methods (Achim et al., 2003; Nasri and Nezamabadi-pour, 2009) are two of the most popular frameworks.

Image deconvolution is the process of restoring the true image from the degraded one. Here the degradation is mainly caused by optical and atmosphere PSF (Point Spread Function). To restore remote sensing images, the MTF (Modulation Transfer Function) based methods are most commonly used. Some representative references address the deconvolution problems of TM (Arbel et al., 2004), SPOT (Pinilla Ruiz and Ariza Lopez, 2002), IKONOS (Ryan et al., 2003) and CBERS-2 (Papa et al., 2008). The Wiener filter (Hillery and Chin, 1991) is a widely employed method to restore the image after the estimation of MTF.

The correction of image stripes is commonly called image destriping. The simplest destriping technique is to process the image data with a low-pass filter in the frequency domain using the discrete Fourier transform (DFT) (Chen et al., 2003). Some researchers remove the stripes using wavelet analysis, which takes advantage of the scaling and directional properties to detect and eliminate striping patterns (Torres and Infante, 2001; Chen et al.,

---

* Corresponding author. Tel.: +86 13908639199; fax: +86 2768778893.
E-mail addresses: shenhf@whu.edu.cn (H. Shen), yaolin610@163.com (Y. Liu), Tinghua_ai@163.net, tinghuaai@gmail.com (T. Ai), freemanwy@hotmail.com (Y. Wang), wavelet778@sohu.com (B. Wu).

0303-2434/$ – see front matter © 2010 Elsevier B.V. All rights reserved.
doi:10.1016/j.jag.2010.04.002

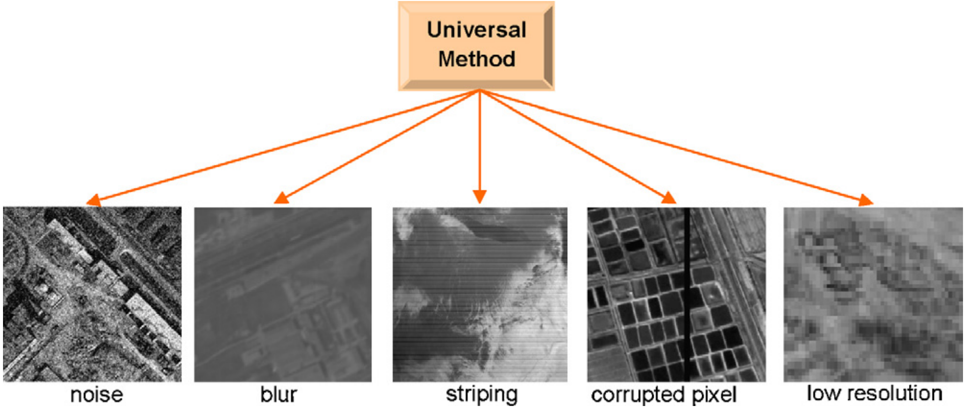

Fig. 1. The functions of the proposed method.

2006). Another destriping approach examines the distribution of digital numbers for each sensor, and adjusts this distribution to some reference distribution. There are also equalization methods (Algazi and Ford, 1981), moment matching (Gadallah et al., 2000), and histogram matching (Rakwatin et al., 2007) methods that are based on the assumption of homogeneous targets, the same mean and standard deviation and the same histogram distribution of each scanning line.

Image inpainting is the technique to recover corrupted pixels in the image. This technique is also called pixel replacement. For this problem, the nearest neighbour, average, or median value replacement methods are commonly employed (Ratliff et al., 2007). Wang et al. (2006) provide a method to retrieve Aqua MODIS band 6 using other bands based on their relationships in Terra MODIS. It is worth noting that there are a number of robust inpainting techniques (Bertalmio et al., 2003; Chan et al., 2003; Grossauer, 2004; Elad et al., 2005) which have not been applied to remote sensing image processing.

To increase the number of pixels in an image, single frame interpolation techniques have been researched extensively. These include nearest neighbour, bilinear and various cubic spline interpolation methods (Chen and de Figueiredo, 1993; Hou and Andrews, 1978; Karayiannis and Venetsanopoulos, 1991; Parker et al., 1983). The traditional interpolation methods often suffer from blurred edges or introduce artefacts around edges. To improve the subjective quality of interpolated images, Bayesian (Schultz and Stevenson, 1994), POCS (Projection-Onto-Convex-Set) (Ratakonda and Ahuja, 1998) and edge-directed interpolation schemes (Wang and Ward, 2001; Li and Orchard, 2001) have been widely researched. Using these methods, the sharp edges can be preserved either by employing an effective prior model or interpolating along the edges detected in advance.

Super-resolution image reconstruction refers to a process that produces a high spatial resolution image from several low resolution images using the non-redundant information among them. The first multi-frame SR idea in (Lee, 1980) was motivated by the requirement to improve the spatial resolution of Landsat TM images. In 2002, CNES (National Space Study Centre, France) successfully launched SPOT5, which could deliver a 2.5 m spatial resolution panchromatic image through the SR processing of two 5 m spatial resolution images (Latry and Rouge, 2003). Shen et al. (2009) proposed an image reconstruction algorithm for multi-temporal MODIS images, and Merino and Nunez (2007) proposed a variable pixel linear reconstruction based method and applied it to Landsat ETM+ images.

The image processing techniques mentioned above are highly related, but few studies so far have attempted to solve the related problems using one model. In this paper, we present a universal image reconstruction method to solve all the posed problems shown in Fig. 1. A universal image observation model is developed to relate the desired image to the degraded image by considering most of the degradations. Based on the observation model, a universal image construction model is set up using the MAP framework. The gradient descent algorithm is employed to carry out the optimization. The main objective of this paper is to validate the universal applicability of the proposed reconstruction method for different image processing problems such as denoising, deconvo-

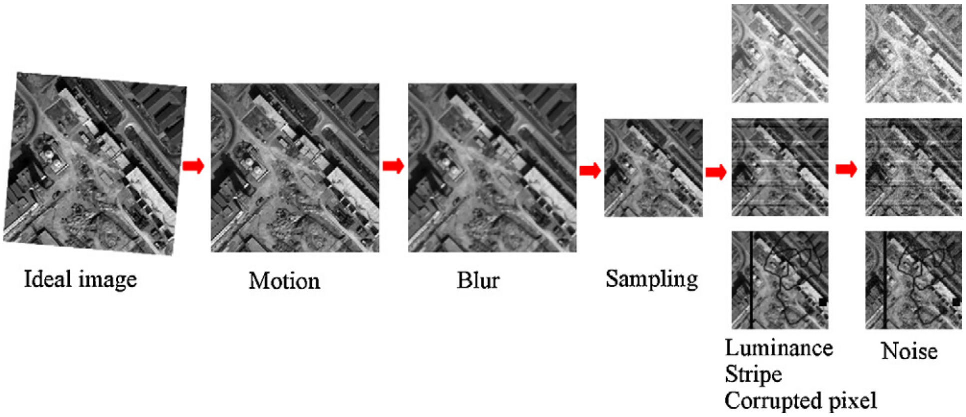

Fig. 2. Illustration of image degradation processes.

lution, destriping, inpainting, interpolation and super-resolution reconstruction.

2. Universal image observation model

To solve the inverse problems of image processing, it is advisable to first analyse the degradation process and assume an image observation model to relate the desired image to the degraded images. This section provides a universal observation equation, which can model most image degradations found in remote sensing acquisitions. The degradation process is illustrated in Fig. 2, and the corresponding observation model is shown in Eq. (1).

$$\boldsymbol{g}_k = \boldsymbol{G}_k\boldsymbol{D}_k\boldsymbol{H}_k\boldsymbol{M}_k\boldsymbol{z} + \boldsymbol{B}_k + \boldsymbol{n}_k \tag{1}$$

Suppose the first left image of Fig. 2 is the ideal or desired image, and we use $\boldsymbol{z}$ to denote it. In ideal conditions, the observed image $\boldsymbol{g}_k$ (k denotes the sequence number of observation) represents $\boldsymbol{z}$. However, the image may be affected by several degradations during image acquisition, transmission and even by unexpected processing and storage. The first degradation is the geometric motion. Considering the same projected coordinate system, the motions between multi-temporal images mainly come from different viewing directions and angles. In Eq. (1), matrix $\boldsymbol{M}_k$ is used to denote the motion operator. The second degradation is the image blurring $\boldsymbol{H}_k$ caused by PSF of the sensor and/or atmosphere. The next is the effect of down-sampling, decided by the number of sensor detectors. We denote the down-sampling operator as $\boldsymbol{D}_k$. Then, there are the three intensity-related effects of global luminance change, periodic stripes and random corrupted pixels. For simplicity, it is assumed that these degradations can be linearly described, but the existence of a linear-assumption error is permitted. We use $\boldsymbol{G}_k$ and $\boldsymbol{B}_k$ to model the intensity-related effects, and these elements denote the gain and offset parameters, respectively ($\boldsymbol{G}_k$ is diagonal). The last term $\boldsymbol{n}_k$ in (1) denotes the sum of sensor noise and model error.

In the universal model (1), if the four matrices $\boldsymbol{G}_k$, $\boldsymbol{D}_k$, $\boldsymbol{H}_k$ and $\boldsymbol{M}_k$ are all identity matrices, and $\boldsymbol{B}_k$ is a zero vector, namely, only considering the noise degradation, the model can be simplified as (2) for image denoising.

$$\boldsymbol{g} = \boldsymbol{z} + \boldsymbol{n} \tag{2}$$

Here, k is ignored as only one observed image is considered.

Based on (2), if the blurring $\boldsymbol{H}$ is further considered, the following special model can be used for image deconvolution.

$$\boldsymbol{g} = \boldsymbol{H}\boldsymbol{z} + \boldsymbol{n} \tag{3}$$

Eq. (4) is the special model for image interpolation, where the down-sampling matrix $\boldsymbol{D}$ is considered.

$$\boldsymbol{g} = \boldsymbol{D}\boldsymbol{z} + \boldsymbol{n} \tag{4}$$

The destriping and inpainting model can be obtained by considering the gain and bias matrices, as shown in (5).

$$\boldsymbol{g} = \boldsymbol{G}\boldsymbol{z} + \boldsymbol{B} + \boldsymbol{n} \tag{5}$$

It is worth noting that the photometric parameters are commonly assumed to be only dependent on the row or column index for image destriping. As for inpainting, if a pixel is corrupted, the corresponding diagonal element of $\boldsymbol{G}$ is zero, and that of $\boldsymbol{B}$ is equal to the pixel value. Otherwise, the diagonal elements of $\boldsymbol{G}$ and $\boldsymbol{B}$ are respectively 1 and 0 for uncorrupted pixels.

Motion based SR reconstruction requires that there are subpixel shifts between the observed images. Therefore, the motion operator $\boldsymbol{M}_k$ must be considered in the observation model. Furthermore, the sun zenith angle and atmospheric absorption and scattering may also bring different intensity ($\boldsymbol{G}_k$ and $\boldsymbol{B}_k$) and blur ($\boldsymbol{H}_k$) effects to the image. Under these considerations, the observation model of SR reconstruction is given by (6).

$$\boldsymbol{g}_k = \boldsymbol{G}_k\boldsymbol{D}\boldsymbol{H}_k\boldsymbol{M}_k\boldsymbol{z} + \boldsymbol{B}_k + \boldsymbol{n}_k \tag{6}$$

We have deduced that the universal observation model (1) can be used for several image improvement techniques, including denoising, deconvolution, interpolation, destriping, inpainting and super-resolution reconstruction. For simplicity, we combine the first four matrices into one matrix as follows:

$$\boldsymbol{g}_k = \boldsymbol{A}_k\boldsymbol{z} + \boldsymbol{B}_k + \boldsymbol{n}_k \tag{7}$$

3. Universal image reconstruction model

Generally, the inverse problems tackled in this paper are all ill-posed because it is necessary to recover a high-quality image from one or several degraded images. Therefore, a difficulty is the multiplicity of possible solutions. In order to obtain more desirable results, the ill-posed problem should be stabilized. Traditionally, regularization has been described from both the algebraic and statistical perspectives. Here we formulate the problem using the MAP framework.

Let the full set of P observed images be denoted by $\boldsymbol{g} = \{\boldsymbol{g}_1, \boldsymbol{g}_2, \ldots \boldsymbol{g}_P\}$. The purpose is to realize the MAP estimate of desired image $\boldsymbol{z}$, given the observed images $\boldsymbol{g}$. The estimate can be computed by

$$\hat{\boldsymbol{z}} = \arg\max_{\boldsymbol{z}} p(\boldsymbol{z}|\boldsymbol{g}) \tag{8}$$

Applying Bayes' rule, Eq. (8) becomes:

$$\hat{\boldsymbol{z}} = \arg\max_{\boldsymbol{z}} \frac{p(\boldsymbol{g}|\boldsymbol{z})p(\boldsymbol{z})}{p(\boldsymbol{g})} \tag{9}$$

Noting that $p(\boldsymbol{g})$ is not a function of $\boldsymbol{z}$, it can be removed from the function. Assuming the observed images are independent, we obtain:

$$\hat{\boldsymbol{z}} = \arg\max_{\boldsymbol{z}} \left[\prod_k p(\boldsymbol{g}_k|\boldsymbol{z})\right] p(\boldsymbol{z}) \tag{10}$$

3.1. Likelihood density function

In (10), $p(\boldsymbol{g}_k|\boldsymbol{z})$ is the likelihood density function, which provides a measure of the conformance of the estimated image to the observed image according to the image observation model. It is determined by the probability density of the noise vector. Using the notation $N(\mu, \boldsymbol{C})$ for a normal distribution with mean μ and covariance $\boldsymbol{C}$, the noise $\boldsymbol{n}_k$ can be modelled as a zero mean Gaussian process.

$$\boldsymbol{n}_k \sim N(0, \boldsymbol{C}_k) \tag{11}$$

Since $\boldsymbol{n}_k = \boldsymbol{g}_k - \boldsymbol{A}_k\boldsymbol{z} - \boldsymbol{B}_k$, the probability distribution function $p(\boldsymbol{g}_k|\boldsymbol{z}) = p(\boldsymbol{n}_k)$ can be denoted as

$$p(\boldsymbol{g}_k|\boldsymbol{z}) = \frac{1}{M_1}\exp\left\{-\frac{1}{2}(\boldsymbol{g} - \boldsymbol{A}_k\boldsymbol{z} - \boldsymbol{B}_k)^T {\boldsymbol{C}_k}^{-1}(\boldsymbol{g} - \boldsymbol{A}_k\boldsymbol{z} - \boldsymbol{B}_k)\right\} \tag{12}$$

where M_1 is a constant. When the noise is assumed to be independent, $\boldsymbol{C}_k$ is actually a diagonal matrix containing the noise variances. Thus, the function can be rewritten as

$$p(\boldsymbol{g}_k|\boldsymbol{z}) = \frac{1}{M_1}\exp\left\{-\frac{1}{2}\left\|\boldsymbol{Q}_k(\boldsymbol{g}_k - \boldsymbol{A}_k\boldsymbol{z} - \boldsymbol{B}_k)\right\|_2^2\right\} \tag{13}$$

where $\boldsymbol{Q}_k$ is a diagonal matrix satisfying $q_{ii} = 1/\sqrt{c_{ii}}$, where q_{ii} and c_{ii} are respectively the diagonal elements of $\boldsymbol{Q}_k$ and $\boldsymbol{C}_k$.

In the Gaussian distribution of (13), $\|\cdot\|_2^2$ denotes the L_2 norm. Another choice for this term is the L_1 norm $\left\|\boldsymbol{Q}_k(\boldsymbol{g}_k - \boldsymbol{A}_k\boldsymbol{z} - \boldsymbol{B}_k)\right\|_1$, which is often used from the algebraic perspective. In this case $\boldsymbol{Q}_k$

represents the weights of all pixels. Generally, the L_1 norm function has some robustness to noise and outliers, but the minimization can only be accomplished by some direct search methods, which often results in local minima. The L_2 norm based Gaussian function is employed in this paper.

3.2. Prior density function

The second density function $p(\boldsymbol{z})$ in Eq. (10) is the image prior, which imposes the spatial constraints on the image. This may include constraints such as positivity, smoothness, etc. (Borman and Stevenson, 1998). Generally, $p(\boldsymbol{z})$ is commonly assumed as the Gibbs form

$$p(\boldsymbol{z}) = \frac{1}{M_2}\exp\left(-\frac{1}{\beta}U(\boldsymbol{z})\right) \tag{14}$$

where M_2 is a constant, β is an adjusting factor often called the "temperature" parameter, and $U(\boldsymbol{z})$ is the prior energy function. Traditionally, the Laplacian prior and Gauss–Markov prior are commonly employed in the fields of image restoration and reconstruction. They regularize the corresponding ill-posed problem by forcing spatial smoothness on the image. Their energy functions are respectively

$$U(\boldsymbol{z}) = \left\|\boldsymbol{L}\boldsymbol{z}\right\|^2 \tag{15}$$

and

$$U(\boldsymbol{z}) = \sum_{x,y}\sum_{c\in C}\rho(d_c(z_{x,y})) \tag{16}$$

where $\boldsymbol{L}$ represents the 2-D Laplacian operation, c is a local group of points called clique within the set of all image cliques C, the quantity $d_c(z_{x,y})$ is a spatial activity measure to pixel $z_{x,y}$, which is often formed by first-order or second-order differences, $\rho(\cdot)$ is the quadratic potential function

$$\rho(i) = i^2 \tag{17}$$

A common criticism of these prior models is that the sharp edges and detailed information in the estimates tend to be overly smoothed. This problem is more obvious when the images are contaminated by noise. A popular edge-preserving prior is the total variation (TV) model, whose energy functional looks like (Rudin et al., 1992)

$$U(\boldsymbol{z}) = \sum_{x}\sum_{y}\sqrt{\left|\nabla z_{x,y}\right|^2 + \gamma} \tag{18}$$

Here, ∇ is the gradient operator, and γ is a small positive parameter that ensures the differentiability. The TV model has been widely used in the image processing field because it is robust and preserves the sharp edges in the image. However, for low spatial resolution remote sensing images in which sharp edges often do not exist, the performance of the TV model has not been validated.

In this paper, we employ the Huber–Markov image prior model. The difference between the Huber–Markov prior and the Gauss–Markov prior is only the potential function $\rho(\cdot)$. The Huber function is defined as

$$\rho(i) = \begin{cases} i^2 & |i| \le \mu \\ 2\mu|i| - \mu^2 & |i| > \mu \end{cases} \tag{19}$$

where μ is a threshold parameter separating the quadratic and linear regions (Schultz and Stevenson, 1996). The advantage of the Huber–Markov model is that it can adjust the penalty function by μ according to the edge activity of the image. When μ approaches $+\infty$, it is the Gauss–Markov prior. Contrarily, when μ approaches 0, it has a similar function to the TV model or L_1 -norm-based models. As for the $d_c(z_{x,y})$ in (16), the following finite second-order differences are computed in four adjacent cliques for every location (x, y) in the image:

$$d_c^1(z_{x,y}) = z_{x-1,y} - 2z_{x,y} + z_{x+1,y} \tag{20}$$

$$d_c^2(z_{x,y}) = z_{x,y-1} - 2z_{x,y} + z_{x,y+1} \tag{21}$$

$$d_c^3(z_{x,y}) = \frac{1}{\sqrt{2}}\left[z_{x-1,y-1} - 2z_{x,y} + z_{x+1,y+1}\right] \tag{22}$$

$$d_c^4(z_{x,y}) = \frac{1}{\sqrt{2}}\left[z_{x-1,y+1} - 2z_{x,y} + z_{x+1,y-1}\right] \tag{23}$$

3.3. Reconstruction model and optimization

Substituting (12) or (13), (14), (16) and (19) in (10), implementing the logarithm function and performing some manipulations, M_1, M_2 can be safely dropped, and the maximization of the posterior probability distribution is equivalent to the regularized minimum problem

$$\hat{\boldsymbol{z}} = arg\min\left\{\lambda\sum_k(\boldsymbol{g}_k - \boldsymbol{A}_k\boldsymbol{z} - \boldsymbol{B}_k)^T\boldsymbol{C}_k^{-1}(\boldsymbol{g}_k - \boldsymbol{A}_k\boldsymbol{z} - \boldsymbol{B}_k) + \sum_{x,y}\sum_{c\in C}\rho(d_c(z_{x,y}))\right\} \tag{24}$$

or

$$\hat{\boldsymbol{z}} = arg\min\left\{\lambda\sum_k\left\|\boldsymbol{Q}_k(\boldsymbol{g}_k - \boldsymbol{A}_k\boldsymbol{z} - \boldsymbol{B}_k)\right\|_2^2 + \sum_{x,y}\sum_{c\in C}\rho(d_c(z_{x,y}))\right\} \tag{25}$$

Here, $\lambda = \beta/2$ is the regularization parameter. It has been mentioned that the matrix $\boldsymbol{Q}_k$ is diagonal and its elements represent the reciprocals of the noise standard deviation in different pixel locations. For convenience, the element values are scaled to the range of 0–1. The difference caused by the scaling can be balanced by λ. Thus the function of $\boldsymbol{Q}_k$ can be regarded as the relative adjustment of regularization at each pixel location in the kth image.

The gradient descent optimization method is used for the minimum problem. Differentiating the cost function (24) and (25) with respect to $\boldsymbol{z}$, we have

$$\boldsymbol{r} = -2\lambda\sum_k\boldsymbol{A}_k^T\boldsymbol{C}_k^{-1}(\boldsymbol{g}_k - \boldsymbol{A}_k\boldsymbol{z} - \boldsymbol{B}_k) + \boldsymbol{r}' \tag{26}$$

and

$$\boldsymbol{r} = -2\lambda\sum_k\boldsymbol{A}_k^T\boldsymbol{Q}_k^T\boldsymbol{Q}_k(\boldsymbol{g}_k - \boldsymbol{A}_k\boldsymbol{z} - \boldsymbol{B}_k) + \boldsymbol{r}' \tag{27}$$

where $\boldsymbol{r}'$ is the derivative of the regularization term that can be solved on a pixel-by-pixel basis. Then, the desired image is solved by employing the successive approximations iteration

$$\hat{\boldsymbol{z}}_{n+1} = \hat{\boldsymbol{z}}_n - \beta_n\boldsymbol{r}_n \tag{28}$$

where n is the iteration number, and β_n is the step size. By making a second-order Taylor series approximation of the objective function at the current state $\hat{\boldsymbol{z}}_n$, a quadratic step size approximation becomes (Schultz and Stevenson, 1996)

$$\beta_n = \frac{\boldsymbol{r}_n^T\boldsymbol{r}_n}{\boldsymbol{r}_n^T(\nabla^2E)\boldsymbol{r}_n} \tag{29}$$

Table 1
Parameter settings of all experiments.

Test number	Processing Intent	Figure	λ	μ	d	Q_k
Test 1	Denoising	Fig. 3	3	8	1×10^{-7}	Identity matrix
Test 2	Deconvolution	Fig. 4	1000	1	1×10^{-6}	Identity matrix
Test 3	Interpolation	Fig. 5	100	1	1×10^{-6}	Identity matrix
Test 4	Destriping	Figs. 6 and 7	15	5	2×10^{-5}	Eq. (32)
Test 5	Inpainting	Fig. 8	50	60	1×10^{-7}	Eq. (31)
Test 6	Inpainting	Fig. 9	5	60	1×10^{-10}	Eq. (31)
Test 7	Super resolution	Fig. 10	15	1	5×10^{-6}	Eq. (31)

where $\nabla^2 E$ is the Hessian matrix of the cost function. The iteration is terminated when

$$\frac{||\boldsymbol{z}_{n+1} - \boldsymbol{z}_n||^2}{||\boldsymbol{z}_n||^2}| \leq d \tag{30}$$

where d is a predetermined coefficient.

In order to ensure that the solution remains within specified sets and to reduce the feasible solution space, some prior constraints can be placed on the image by performing corresponding projections after the solution of (26). The first is the amplitude constraint whose projection P_1 is defined as

$$P_1[z(x,y)] = \begin{cases} \alpha, & z(x,y) < \alpha \\ z(x,y) & \alpha \leq z(x,y) \leq \beta \\ \beta, & z(x,y) > \beta \end{cases} \tag{31}$$

where α and β are the amplitude bounds. Furthermore, in order to prevent the original information of uncorrupted pixels from being smoothed during the inpainting or destriping process, we assign their values to the original observed ones at the end of each iteration by projection P_2

$$P_2[z(x,y)] = \begin{cases} z(x,y), & \text{dead or stripe pixels} \\ g(x,y), & \text{healthy pixels} \end{cases} \tag{32}$$

4. Experimental results

To test the performance of the proposed method, we conducted a series of experiments for denoising, deconvolution, interpolation, destriping, inpainting and super-resolution reconstruction. The parameter settings are shown in Table 1. The regularization parameter λ, Huber threshold μ and iteration termination parameter d are determined heuristically. Since we assume the noise is identically distributed in image denoising, deconvolution and interpolation, the matrix $\boldsymbol{Q}_k$ in (25) is an identity matrix in these cases. For image inpainting and super-resolution reconstruction, the corresponding elements of corrupted pixels and outliers (pixels which strongly deviate from the registration model) are set to 0, and other diagonal elements are set to 1, i.e. it satisfies

$$q_{ii} = \begin{cases} 0 & \text{dead or outlier pixels} \\ 1 & \text{otherwise} \end{cases} \tag{33}$$

For pixels on the stripes, the following equation is used to determine the diagonal elements in Q_k

$$q_{ii} = \ln\left[\frac{(e-1)(std - \min)}{\max - \min} + 1\right] \tag{34}$$

where *std* represents the standard deviation. It is worth noting that the *std* value should be computed on a neighbouring region that does not contain any stripes or corrupted pixels. *max* and *min* are the *std* thresholds corresponding to the maximum value 1 and minimum value 0. They are set to 3 and 250 respectively in this paper. Eq. (34) ensures that larger element values are chosen for sharp regions to retain the high frequency information.

4.1. Image denoising

Fig. 3 shows the experimental results of image denoising. Fig. 3(a) is the noisy image simulated by adding Gaussian noise to an original image. Fig. 3(b) is the denoised result using a common Gaussian filter. It is seen that the edge information in the image has been overly smoothed with the denoising process. In contrast, the proposed algorithm is preferable because it can provide simultaneous denoising and edge preservation, as shown in Fig. 1(c). The PSNR (peak signal to noise ratio) values of Fig. 3(b) and (c) are 22.21 and 23.17 dB, respectively.

4.2. Image deconvolution

In the blurring experiment, the proposed algorithm was performed on an original CBERS-2 (China-Brazil Earth Resource Satellite) sub-image, which is shown in Fig. 4(a). This image is strongly blurred by the PSF of the imaging sensor and atmosphere. Fig. 4(b) is the deblurred image, and Fig. 4(c) and (d) are the contrast enhanced results of Fig. 4(a) and (b). It is seen that the deblurred image is much clearer than the observed one. The image average gradients of Fig. 4(a) and (b) are 3.7 and 7.1. Fig. 4(c) and (d) are respectively the contrast enhancement of Fig. 4(a) and (b).

4.3. Image interpolation

In the interpolation experiment, an aerial image was first down-sampled by a factor of 2 in both dimensions. The down-sampled

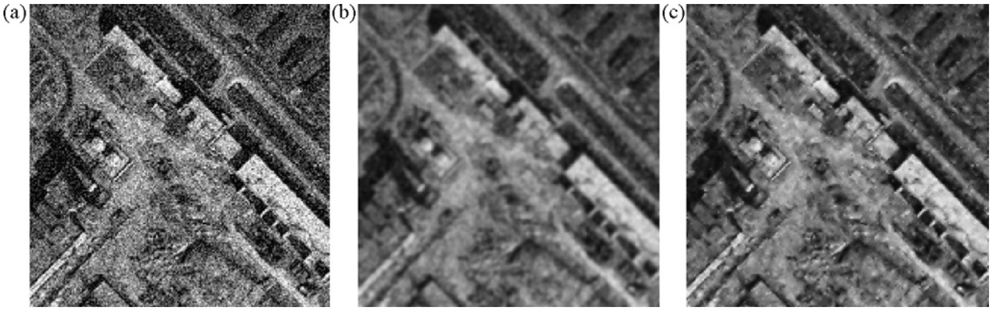

Fig. 3. Denoising experiment. (a) The noisy image, (b) denoised image using Gaussian filter, and (c) denoised image using the proposed algorithm.

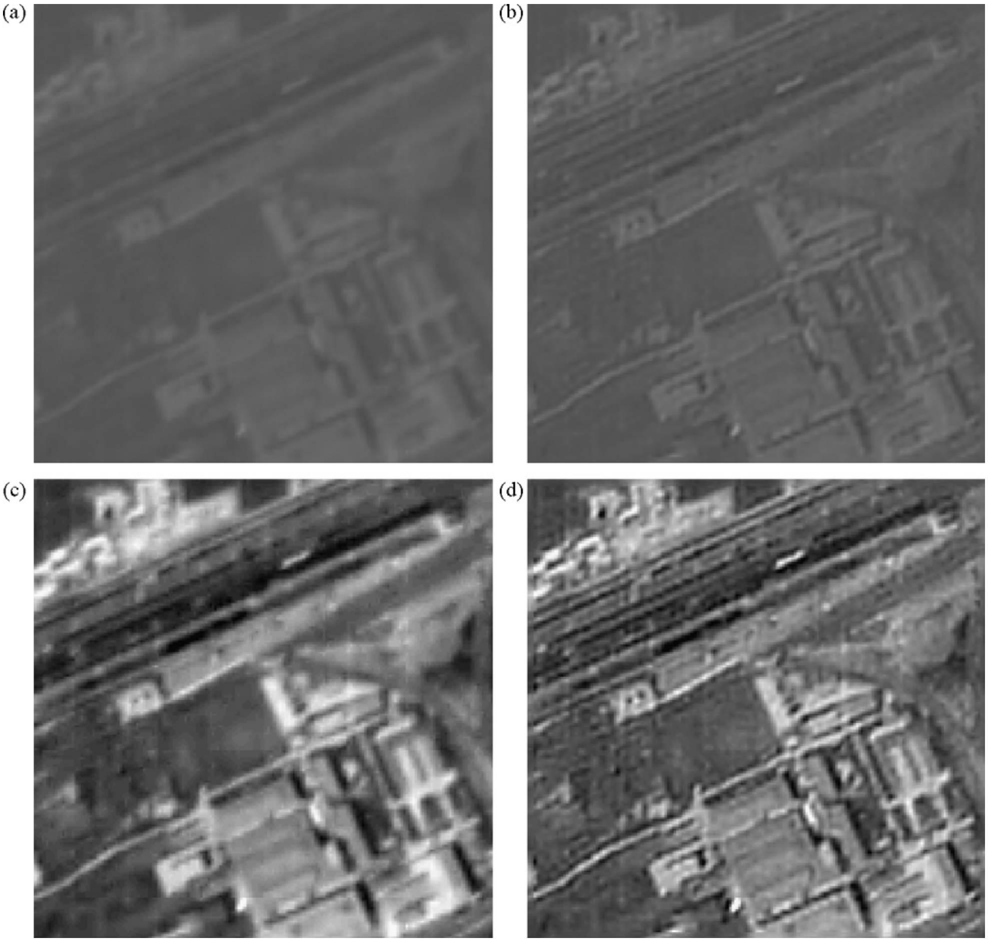

Fig. 4. Deconvolution experiment on a CBERS-2 image. (a) The observed image, (b) the deblurred image, (c) contrast enhanced result of the observed image, and (d) contrast enhanced result of the deblurred image.

image was interpolated to the original size using the cubic interpolation method and the proposed method. These images are shown in Fig. 5. By comparison, we can see the proposed method provides more desirable results with sharper edges and more detailed information than with the traditional cubic interpolation. The PSNR values of Fig. 5(b) and (c) are 24.63 and 25.82 dB, respectively.

4.4. Image destriping

The destriping experiment was performed on a MODIS (Moderate Resolution Imaging Spectrometer) image. The Aqua MODIS band 30 data acquired on 26 December 2003 was used, and a subimage is shown in Fig. 6(a). To make a comparative analysis, the moment matching, histogram matching and the proposed destriping methods were implemented. The destriped results are shown in Fig. 6(b)–(d). Fig. 7 shows the detailed regions around the lake of the destriped results of the different methods. Experimental results indicate that moment matching and histogram matching can remove most stripes, but there are still considerable radiance fluctuations within the non-dominated uniform regions. The proposed algorithm, however, provides a much more robust destriping from the visual perspective.

4.5. Image inpainting

Fig. 8 shows the inpainting experiments for the recovery of vertical corrupted lines. Fig. 8(a) is contaminated by 1 corrupted column that is 8 pixels wide. Fig. 6(b) and (c) are respectively the

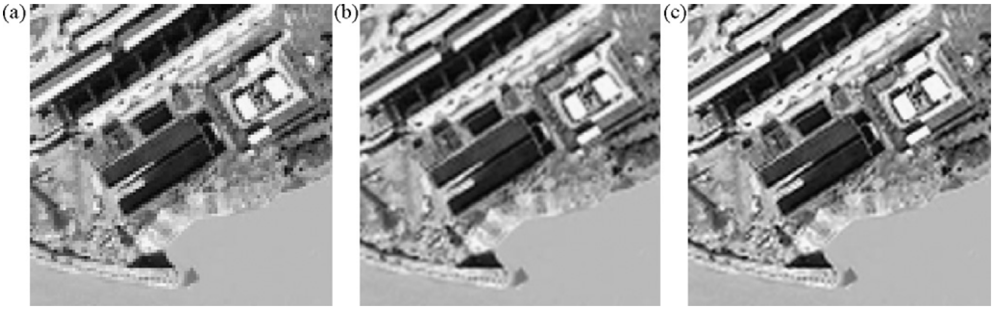

Fig. 5. Interpolation experiment. (a) The down-sampled image, (b) cubic interpolated, and (c) the proposed method.

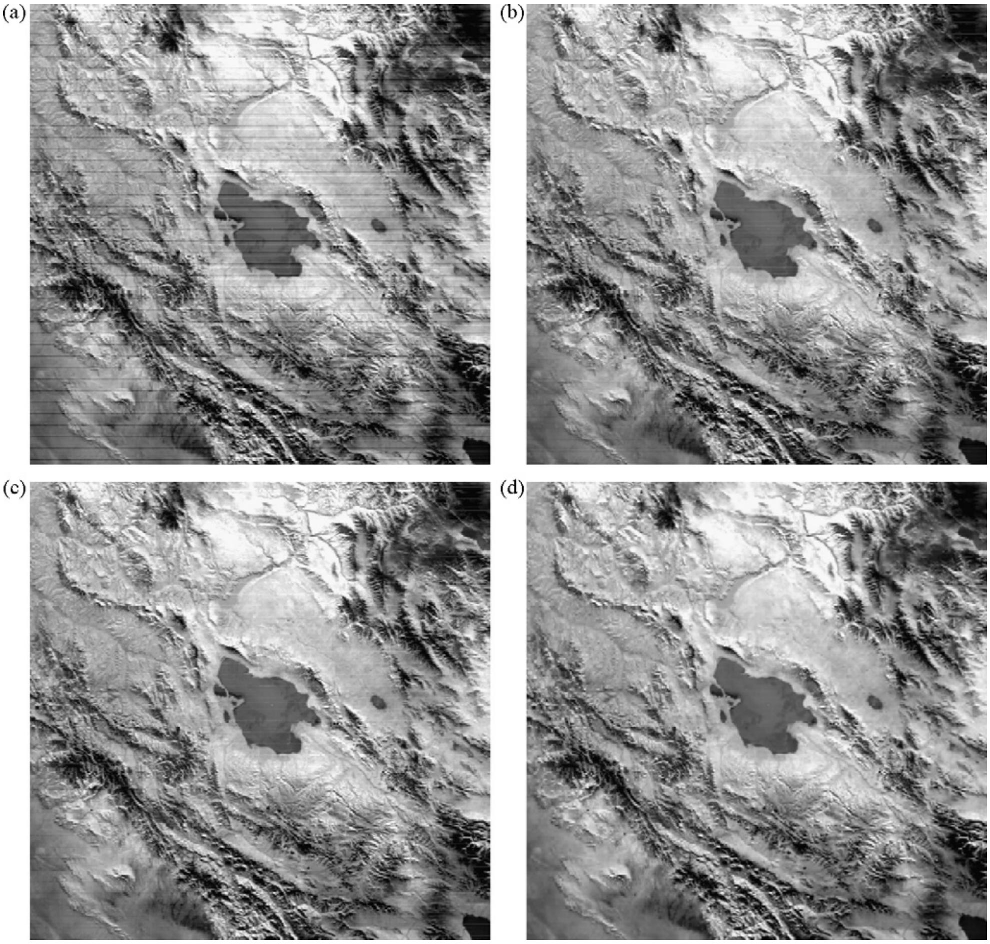

Fig. 6. Destriped results of the Aqua MODIS image. (a) The original image, (b) moment matching, (c) histogram matching, and (d) the proposed algorithm.

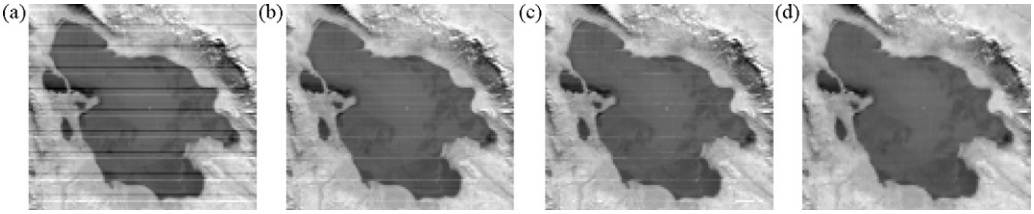

Fig. 7. Detailed lake regions of the destriped results of different methods. (a) The original image, (b) moment matching, (c) histogram matching, and (d) the proposed algorithm.

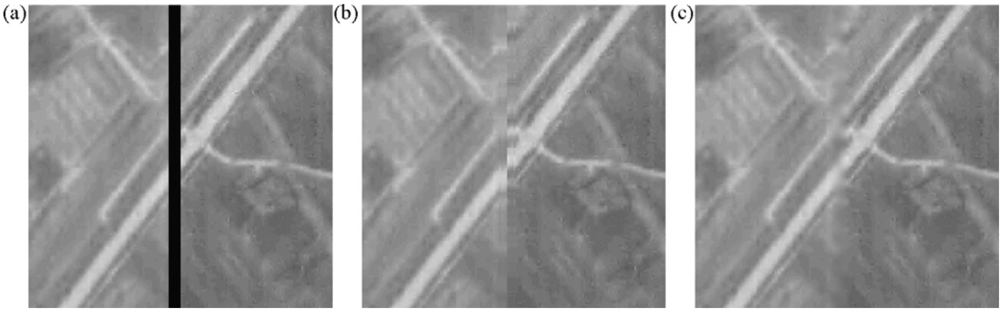

Fig. 8. Inpainting experimental results for the recovery of vertical corrupted lines. (a) Original image contaminated by a corrupted line of 8-pixel width, (b) inpainted image using ENVI 4.4, (c) inpainted image using the proposed algorithm.

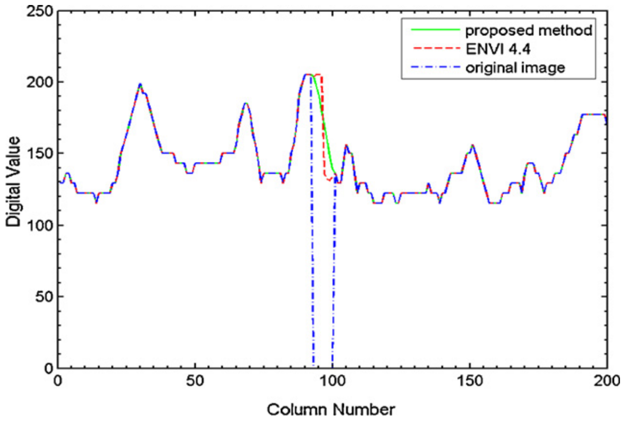

Fig. 9. Horizontal profiles of digital values of the 112th line on each of the images in Fig. 8.

inpainted results using the interpolation based "Replace Bad Lines" function in ENVI 4.4 and the proposed algorithm. It is seen that the conventional interpolation-based method in ENVI 4.4 is not employable for such a wide corrupted line. The proposed algorithm, however, is more robust for the increase in width of the corrupted region. Although the lost information cannot be completely recovered, the visual quality of the result is improved sufficiently. Fig. 9 shows the horizontal profiles of digital values of the 112th line on each of the images in Fig. 8. It is seen that the proposed method produces much gentler easement curve around the corrupted region.

Fig. 10(a) is an original QuickBird image. Fig. 10(b) assumes the image is contaminated by randomly distributed corrupted pixels whose percentage is 90%. In this image no objects can really be seen. The inpainted result is shown in Fig. 10(c). Even although the percentage of corrupted pixels is so high, the ground objects can still be distinguished from the inpainted image. The PNSR of Fig. 10(b) and (c) are respectively 8.17 and 23.24 dB.

4.6. Super-resolution reconstruction

In the experiments, we used six MODIS band-4 images with ground resolution of 500 m. These images were captured from 28 December 2003 to 8 January 2004. Our data processing was restricted to typical 50 by 50 block images in order to reduce the effects of clouds and mosaicing errors. A 3 × 3 Gaussian blur kernel with unit variance was assumed and employed. The original six images are shown in Fig. 11(a)–(f). Fig. 11(g) is the cubic interpolated image. The corresponding super-resolution result is shown in Fig. 11(h).

By visual comparison, it is seen that the results of the proposed SR algorithm are much clearer than those of the cubic interpolation algorithms, the reason being that these results fused the complementary information in different observed images. The image average gradients of Fig. 11(g) and (h) are respectively 18.9 and 29.0.

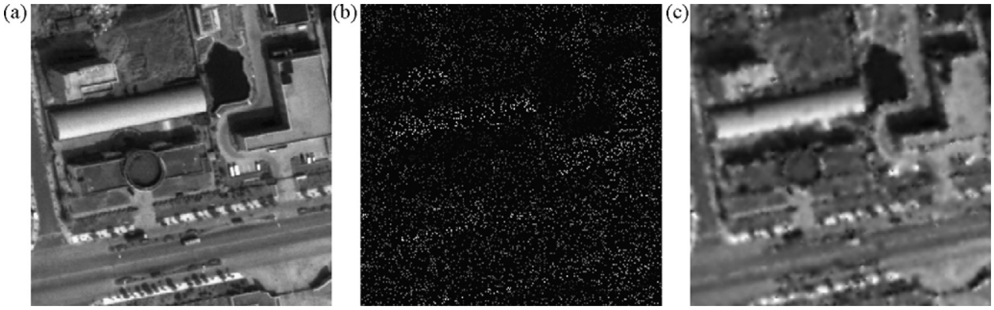

Fig. 10. Inpainting experiment for the recovery of random corrupted pixels. (a) The original QuickBird image, (b) the image contaminated by 90% corrupted pixels, and (c) the inpainted image using the proposed algorithm.

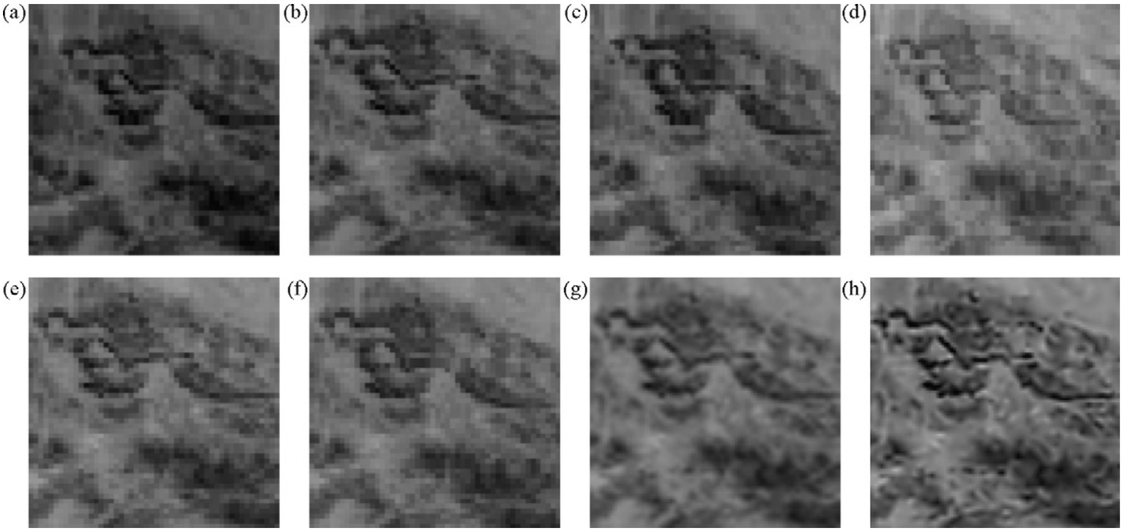

Fig. 11. (a)–(f) Images captured on 28/12/2003, 30/12/2003, 01/01/2004, 04/01/2004, 06/01/2004 and 08/01/2004, respectively, (g) cubic interpolated image, and (h) SR reconstructed image.

5. Conclusions

In order to improve quality and increase the application potential of remote sensing images, this paper presents a universal reconstruction method. This method was developed based on a universal image observation model and MAP framework. The proposed method was tested for image denoising, deconvolution, destriping, inpainting, interpolation and super-resolution reconstruction. Experimental results demonstrate that this method outperforms many other widely used methods for solving the same problems. Nevertheless, further work can potentially expand the method to perform image fusion of different spectral bands.

Acknowledgments

We want to thank the helpful comments and suggestions from the anonymous reviewers. This work was supported by the Major State Basic Research Development Program (973) under Grant 2009CB723905, by the National High Technology Research and Development Program(863) Program of China under Grant 2007AA12Z209, by the National Natural Science Foundation (NSFC) under Grants 40801182, 40971242, 40971220.

References

Achim, A., Tsakalides, P., Bezerianos, A., 2003. SAR image denoising via Bayesian wavelet shrinkage based on heavy-tailed modeling. IEEE Transactions on Geoscience and Remote Sensing 41 (8).

Algazi, V.R., Ford, G.E., 1981. Radiometric equalization of nonperiodic striping in satellite data. Computer Graphics and Image Processing 16 (3), 287–295.

Arbel, D., Cohen, E., Citroen, M., Blumberg, D.G., Kopeika, N.S., 2004. Landsat TM satellite image restoration using Kaiman Filters. Photogrammetric Engineering and Remote Sensing 70 (1), 91–100.

Bertalmio, M., Vese, L., Sapiro, G., Osher, S., 2003. Simultaneous structure and texture image inpainting. IEEE Transactions on Image Processing 12 (8), 882–889.

Borman, S., Stevenson, R., July 1998. Spatial Resolution Enhancement of Low-Resolution Image Sequences: A Comprehensive Review with Directions for Future Research. Laboratory for Image and Signal Analysis (LISA), University of Notre Dame, Report.

Chan, T.F., Kang, S.H., Shen, J.H., 2003. Euler's elastica and curvature-based inpainting. SIAM Journal on Applied Mathematics 63 (January (2)), 564–592.

Chen, G., de Figueiredo, R.J.P., 1993. A unified approach to optimal image interpolation problems based onlinear partial differential equation models. IEEE Transactions on Image Processing 2 (1), 41–49.

Chen, J., Shao, Y., Guo, H., Wang, W., Zhu, B., 2003. Destriping CMODIS data by power filtering. IEEE Transactions on Geoscience and Remote Sensing 41 (9), 2119–2124.

Chen, J.S., Lin, H., Shao, Y., Yang, L.M., 2006. Oblique striping removal in remote sensing imagery based on wavelet transform. International Journal of Remote Sensing 27 (April (8)), 1717–1723.

Elad, M., Starck, J.L., Querre, P., Donoho, D.L., 2005. Simultaneous cartoon and texture image inpainting using morphological component analysis (MCA). Applied and Computational Harmonic Analysis 19 (3), 340–358.

Frost, V.S., Stiles, J.A., Shanmugan, K.S., Holtzman, J.C., 1982. A model for radar images and its application to adaptive digital filtering of multiplicative noise. IEEE Transactions on Pattern Analysis and Machine Intelligence 4, 157–166.

Gadallah, F.L., Csillag, F., Smith, E.J.M., 2000. Destriping multisensor imagery with moment matching. International Journal of Remote Sensing 21 (August (12)), 2505–2511.

Grossauer, H., 2004. A combined PDE and texture synthesis approach to inpainting. Computer Vision—Eccv 2004 3022 (Pt 2), 214–224.

Hillery, A.D., Chin, R.T., 1991. Iterative Wiener filters for image restoration. IEEE Transactions on Signal Processing 39 (8), 1892–1899.

Hou, H., Andrews, H., 1978. Cubic splines for image interpolation and digital filtering. IEEE Transactions on Acoustics, Speech, and Signal Processing [see also IEEE Transactions on Signal Processing] 26 (6), 508–517.

Isar, D., Isar, A., Quinquis, A., 2006. "Multi-scale MAP denoising of SAR Images," Presented at OCEANS Piscataway, NJ 08855-1331, United States.

Karayiannis, N.B., Venetsanopoulos, A.N., 1991. Image interpolation based on variational principles. Signal Processing 25 (3), 259–288.

Kuan, D.T., Sawchuk, A.A., Strand, T.C., Chavel, P., 1985. Adaptive noise smoothing filter for images with signal-dependent noise. IEEE Transactions on Pattern Analysis and Machine Intelligence 7 (2), 165–177.

Latry, C., Rouge, B., 2003. "Super Resolution: Quincunx Sampling and Fusion Processing," Presented at International Geoscience and Remote Sensing Symposium (IGARSS), Toulouse, France.

Lee, J.S., 1980. Digital image enhancement and noise filtering by use of local statistics. IEEE Transactions on Pattern Analysis and Machine Intelligence 2, 165–168.

Li, X., Orchard, M.T., 2001. New edge-directed interpolation. IEEE Transactions on Image Processing 10 (10), 1521–1527.

Merino, M.T., Nunez, J., 2007. Super-resolution of remotely sensed images with variable-pixel linear reconstruction. IEEE Transactions on Geoscience and Remote Sensing 45 (5), 1446–1457.

Nasri, M., Nezamabadi-pour, H., 2009. Image denoising in the wavelet domain using a new adaptive thresholding function. Neurocomputing 72 (4-6), 1012–1025.

Papa, J.P., Mascarenhas, N.D.A., Fonseca, L.M.G., Bensebaa, K., 2008. Convex restriction sets for CBERS-2 satellite image restoration. International Journal of Remote Sensing 29 (2), 443–458.

Parker, J.A., Kenyon, R.V., Troxel, D.E., 1983. Comparison of interpolating methods for image resampling. IEEE Transactions on Medical Imaging 2 (1), 31–39.

Pinilla Ruiz, C., Ariza Lopez, F.J., 2002. Restoring SPOT images using PSF-derived deconvolution filters. International Journal of Remote Sensing 23 (12), 2379–2391.

Rakwatin, P., Takeuchi, W., Yasuoka, Y., 2007. Stripe noise reduction in MODIS data by combining histogram matching with facet filter. IEEE Transactions on Geoscience and Remote Sensing 45 (6), 1844–1856.

Ratakonda, K., Ahuja, N., 1998. "POCS Based Adaptive Image Magnification," Presented at IEEE International Conference on Image Processing, Chicago, IL, USA.

Ratliff, B.M., Tyo, J.S., Boger, J.K., Black, W.T., Bowers, D.L., Fetrow, M.P., 2007. Dead pixel replacement in LWIR microgrid polarimeters. Optics Express 15 (June (12)), 7596–7609.

Rudin, L., Osher, S., Fatemi, E., 1992. Nonlinear total variation based noise removal algorithms. Physica D 60, 259–268.

Ryan, R., Baldridge, B., Schowengerdt, R.A., Choi, T., Helder, D.L., Blonski, S., 2003. IKONOS Spatial Resolution and Image Interpretability Characterization.

Schultz, R.R., Stevenson, R.L., 1994. A Bayesian approach to image expansion for improved definition. IEEE Transactions on Image Processing 3 (3), 233–242.

Schultz, R.R., Stevenson, R.L., 1996. Extraction of high-resolution frames from video sequences. IEEE Transactions on Image Processing 5 (June (6)), 996–1011.

Shen, H., Ng, M.K., Li, P., Zhang, L., 2009. Super resolution reconstruction algorithm to MODIS remote sensing images. The Computer Journal 52 (1), 90–100.

Torres, J., Infante, S.O., 2001. Wavelet analysis for the elimination of striping noise in satellite images. Optical Engineering 40 (July (7)), 1309–1314.

Wang, Q., Ward, R., 2001. "A New Edge-directed Image Expansion Scheme," Presented at IEEE International Conference on Image Processing, Thessaloniki.

Wang, L., Qu, J.J., Xiong, X., Hao, X., Xie, Y., Che, N., 2006. A new method for retrieving band 6 of aqua MODIS. IEEE Geoscience and Remote Sensing Letters 3 (2), 267–270.